Journal of Inorganic Biochemistry 242 (2023) 112162

Contents lists available at ScienceDirect

Journal of Inorganic Biochemistry

journal homepage: www.elsevier.com/locate/jinorgbio

A bioinspired cobalt catalyst based on a tripodal imidazole/pyridine platform capable of water reduction and oxidation

Krista M. Kulesa [a,1], Diego S. Padilha [b,1], Bishnu Thapa [a,1], Shivnath Mazumder [c], Yaroslav Losovyj [d], H. Bernhard Schlegel [a,*], Marciela Scarpellini [b,*], Cláudio N. Verani [a,*]

[a] Department of Chemistry, Wayne State University, 5101 Cass Avenue, Detroit, MI 48202, USA
[b] Instituto de Química, Universidade Federal do Rio de Janeiro, Rio de Janeiro, RJ 21941-611, Brazil
[c] Department of Chemistry, Indian Institute of Technology Jammu, Jammu 181221, India
[d] Department of Chemistry, Indiana University, Bloomington, 800 E. Kirkwood Avenue, Bloomington, IN 47405, USA

ARTICLE INFO

Keywords:
Bioinorganic
Electrocatalysis
Drug carrier repurposed
Cobalt complex
Water reduction
Water oxidation

ABSTRACT

The prototypical drug carrier $[Co^{II}(L^1)Cl]PF_6$ (**1**), where L^1 is a tripodal amine bound to pyridine and methyl-imidazoles, had its electrocatalytic water splitting activity studied under different pH conditions. This species contains a high-spin $3d^7$ Co^{II} metal center, and is capable of generating both H_2 from water reduction and O_2 from water oxidation. Turnover numbers reach 390 after 3 h for water reduction. Initial water oxidation activity is molecular, with TONs of 71 at pH 7 and 103 at pH 11.5. The results reveal that species **1** can undergo several redox transformations, including reduction to the $3d^8$ Co^{I} species that precedes a $^{LS}3d^6$ hydride for water reduction, as well as nominal Co^{IV}═O and Co^{III}-OOH species required for water oxidation. Post-catalytic analyses confirm the molecular nature of reduction and support initial molecular activity for oxidation.

1. Introduction

Catalytic water-splitting is a multielectronic process usually divided into two half-cell reactions, namely oxidation and reduction.

$$\text{Water splitting}: 2H_2O_{(l)} \rightarrow 2H_{2(g)} + O_{2(g)} \quad (1)$$

$$\text{Oxidation}: 2H_2O_{(l)} \rightarrow O_{2(g)} + 4H^+ + 4e^- \quad (2)$$

$$\text{Reduction}: 4H^+ + 4e^- \rightarrow 2H_{2(g)} \quad (3)$$

The first step yields protons that enable the second, and the process is necessary for the development of the Hydrogen Economy, being heavily inspired by dioxygen generation in the Photosystem II [1,2,3,4,5]. Proton reduction is also observed in hydrogenases, a family of enzymes that serve as inspiration for the above-mentioned catalytic processes [6,7]. A common feature for these enzymes is the use of active sites that rely on Earth-abundant 3*d* metals. For instance, both water reduction and proton reduction have been successfully realized by a limited number of bioinspired molecular catalysts featuring Mn^{II}, Fe^{II}, $Co^{II/III}$, Ni^{II}, and Cu^{II} [8,9,10,11,12,13], where low-valent states such as $3d^8$ Co^{I}, $3d^9$ Ni^{I}, or $3d^{10}$ Cu^{I} must be achieved to enable the required hydride formation that precedes H_2 evolution [14,15,16,17,18]. The process is described stepwise as follows:

Abbreviations: 6–31+G(d,p), Standard, split-valence double-zeta basis set, with (d,p) polarization functions; %F, Faradaic efficiency; B3LYP*, Becke 3-Parameter, Lee, Yang & Parr density functional; DFT, Density Functional Theory; DCM, Dichloromethane; DLS, Dynamic light scattering; EDX, Energy dispersive X-ray spectroscopy; FTO, Fluorine-dopped tin oxide; L^1, tripodal amine bound to pyridine and methyl-imidazoles; MeCN, Acetonitrile; MeOH, Methanol; MO_x, Generic metal oxides; PCET, Proton-coupled electron transfer; SDD, Stuttgart-Dresden and D95 basis set; SEM, Scanning electron microscopy; sh, Shoulder in spectroscopic band; SMD-SCRF, Solvation model density – solvent cavity reaction field; $TBAPF_6$, Tetrabutylammonium hexafluorophosphate; TON, Turnover number; TOF, Turnover frequency; V *vs.* Ag/AgCl, Electrochemical potential in Volts *vs.* the silver/silver chloride electrode; V *vs.* Fc/Fc+, Electrochemical potential in Volts *vs.* the internal standard ferrocene/ferrocenium; V *vs.* NHE, Electrochemical potential in Volts *vs.* the normal hydrogen electrode; V *vs.* RHE, Electrochemical potential in Volts *vs.* the reversible hydrogen electrode; XPS, X-ray photoelectron spectroscopy.

* Corresponding authors.
E-mail addresses: hbs@chem.wayne.edu (H.B. Schlegel), marciela@iq.ufrj.br (M. Scarpellini), claudio.verani@wayne.edu (C.N. Verani).
[1] Current addresses: K.M.K.: Department of Chemistry, Indiana University, Bloomington, IN, 47405, USA; D.S.P.: Nortec Química, Duque de Caxias, RJ, 25250, Brazil; B.T.: Eli Lilly and Company, Indianapolis, IN, 46225, USA.

https://doi.org/10.1016/j.jinorgbio.2023.112162
Received 17 September 2021; Received in revised form 4 February 2023; Accepted 13 February 2023
Available online 15 February 2023

$$\text{Reduction of trivalent metal}: \left[LM^{III}\right]^{3+} + e^- \rightarrow \left[LM^{II}\right]^{2+} \quad (4)$$

$$\text{Reduction of bivalent metal}: \left[LM^{II}\right]^{2+} + e^- \rightarrow \left[LM^{I}\right]^{+} \quad (5)$$

$$\text{Hydride formation}: \left[LM^{I}\right]^{+} + H^+ \rightarrow \left[LM^{III} - H^-\right]^{2+} \quad (6)$$

Electrocatalytic systems usually involve a second reduction driven by the overpotential of the electrode, forming $[LM^{II}\text{-}H^-]^+$ prior to dihydrogen formation either by heterolytic or homolytic pathways described as follows:

$$\text{Heterolytic pathway}: \left[LM^{II} - H^-\right]^{+} + H^+ \rightarrow \left[LCo^{II}\right]^{2+} + H_2 \quad (7)$$

$$\text{Homolytic pathway}: \left[LM^{II} - H^-\right]^{+} + \left[LM^{II} - H^-\right]^{+} \rightarrow 2\left[LM^{I}\right]^{2+} + H_2 \quad (8)$$

When $3d^n$ metal ions promote water oxidation, high-valent species of appropriate geometry are required *via* subsequent oxidations and deprotonations described as follows:

$$\left[LM^{III} - OH_2\right]^{3+} \rightarrow \left[LM^{IV} - OH\right]^{3+} + e^- + H^+ \quad (9)$$

$$\left[LM^{IV} - OH\right]^{3+} \rightarrow \left[LM^{V} = O\right]^{3+} + e^- + H^+ \quad (10)$$

Although complex reactions have been documented [19], subsequent release of O_2 usually favors either water nucleophilic attack or oxyl radical coupling [20,21,22,23,24,25,26,27]. The first pathway describes the attack of a water molecule to an oxidized metal-oxo/oxyl (M = O) group, resulting in a hydroperoxo (M-OOH) intermediate. The second describes the intramolecular coupling of two individual metal-oxo/oxyl species to form bridged (M-O_2-M), or terminal (M-O_2) peroxo intermediates. A recent report demonstrated the feasibility of side-on peroxides, increasing the complexity of these pathways [28].

Catalysts based on 4*d* and 5*d* metals have led to successful water oxidation because higher oxidation states are stabilized in low-spin pseudo-octahedral ligand fields. This leads to the depopulation of the t_{2g}-like molecular orbitals with metallic character, *e.g.* $^{LS}4d^6$ Ru^{II} $[t_{2g}^6]$ converts to $^{LS}4d^4$ Ru^{IV}=O $[t_{2g}^4]$ without involvement of the empty e_g-like MOs of higher energy. The use of 3*d* metals is expected to yield more affordable water oxidation associated with the depopulation of orbitals in smaller ligand fields [29,30]. However, ligand degradation in the form of methylene oxidation can lead to the formation of catalytic MO_x nanoparticles. This issue has imposed severe limitations to the development of the field and several known Mn-, Fe-, and Co-based catalysts have shown such degradation [31,32].

A few catalysts are capable of promoting both water reduction *and* oxidation independently [33,34], showing that ligand design is a relevant tool in the development of catalysts that display affordable redox potentials to reach a panoply of low- and high-valent species [35]. These potentials are sometimes attained *via* ligand involvement [36,37,38], thus mitigating the need for extreme oxidation states such as M^{IV} or M^{V} by the formation of $[M^{III}L^{\bullet}]$ and $[M^{III}L^{\bullet\bullet}]$ intermediates that delocalize the electronic density in nominally high-valent states.

In this paper we probe the catalytic activity of $[Co^{II}(L^1)Cl]PF_6$ (**1**), shown in Scheme 1. This species was initially designed and studied by the Scarpellini Group [39] as a redox-activated prototype carrier for cytotoxic molecules to attack hypoxic cells, capable of fast azide (N_3^-) release upon reduction with ascorbic acid. The tripodal design resembles that of the bioinorganically relevant ligand tris(methyl-2-pyridin)amine (tmpa) [40]. However, tmpa and other pyridine-rich ligands are prone to ligand degradation during the catalytic cycle [41].

We hypothesize that the replacement of pyridine donors by methyl-imidazoles in L^1 may favor metal-centered low-valence and preclude ligand dissociation during the water reduction cycle, because the in-plane N-based lone pair neither contributes to, nor is affected by ring aromaticity. Although the ligand contains several methylene groups prone to oxidation during oxidative catalytic cycles, we propose that the lone pair of imidazole donors binds more strongly (pKa 6.95) than pyridine (pKa 5.25) to the metal center. This stronger chelation may slow down anticipated catalyst degradation during water oxidation. Indeed, species **1** displays both electrocatalytic water reduction and oxidation behavior; the results follow.

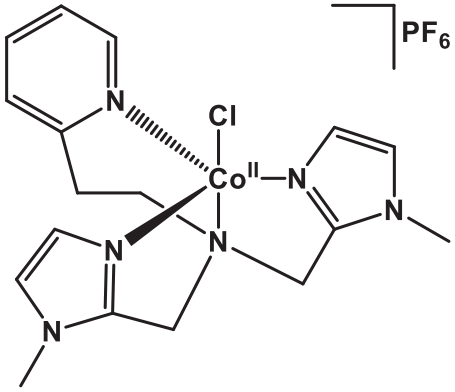

Scheme 1. The catalyst $[Co^{II}(L^1)Cl]PF_6$ (**1**).

2. Results and discussion

Synthetic protocols and structure. The ligand L^1 was originally reported by Scarpellini et al. [42] and obtained as an oil by treatment of a MeOH solution of 2-(2-aminoethyl)pyridine with 1-methyl-2-imidazole-carboxaldehyde at 0 °C, followed by reduction with Pd/C. The compound $[Co^{II}(L^1)Cl]PF_6$ (**1**) was synthesized following procedure by Scarpellini et al. [38], where the ligand L^1 was dissolved in warm MeOH and treated with $CoCl_2{\cdot}6H_2O$, followed by addition of tetrabutylammonium hexafluorophosphate, $TBAPF_6$. The resulting spectroscopic, spectrometric, combustion, and redox analyses were in excellent agreement with reported values. The crystal structure of $[Co^{II}(L^1)Cl]PF_6$ (**1**) has been established and consists of a five-coordinate Co^{II} center, where one $N_{pyridine}$ and two $N_{imidazole}$ donors of the tetradentate L^1 form a trigonal plane; the remaining N_{amine} donor in L^1 is axial to a monodentate chlorido ligand. A PF_6^- counterion is ionically associated to **1** for charge balance. Relevant bond lengths [41] include Co-N_{amine} at 2.426 Å, Co-$N_{pyridine}$ at 2.077 Å, Co-$N_{imidazole}$ at 2.008 and 2.022 Å, as well as Co—Cl at 2.304 Å.

Electronic and electrochemical behavior. UV–visible and electron paramagnetic resonance (EPR) spectroscopies were used along with electrochemical methods in order to follow the electronic changes associated with redox processes relevant to water splitting. The UV–visible spectrum of 10^{-3} M acetonitrile solutions of $[Co^{II}(L^1)Cl]PF_6$ (**1**) showed an absorbance at 265 nm ($\varepsilon \approx 2900\ M^{-1}\ cm^{-1}$) assigned to a $\pi \rightarrow \pi^*$ intraligand charge transfer band. Weak metal-based *d-d* transitions appeared around 520 (150), 560 (sh, 230), and 585 nm (280 $M^{-1}\ cm^{-1}$) and are shown in **Fig. S1**. More relevant, the spectra taken at pHs 7 and 11.5 in aqueous phosphate buffers displayed similar processes at comparable energies, with an intra-ligand charge transfer band shifting slightly from 265 to 263 nm, and the metal-centered bands appearing at 500 and 610 nm. Stability tests at both pHs monitored the robustness of **1** in solution over 8 h. Fig. 1a summarizes this data for pH 11.5. While no major overall shifts in energy or absorption indicated remarkable stability, the low intensity bands observed between 400 and 625 nm deserve attention. The bands at 500 and 610 nm blue-shifted slowly to 495 and 600 nm respectively, while a new band appeared at 400 nm and a shoulder became visible at 625 nm. These changes are attributed to the substitution of the apical ligand from chlorido to hydroxo. No obvious complex demetallation or ligand degradation was observed while in the divalent state.

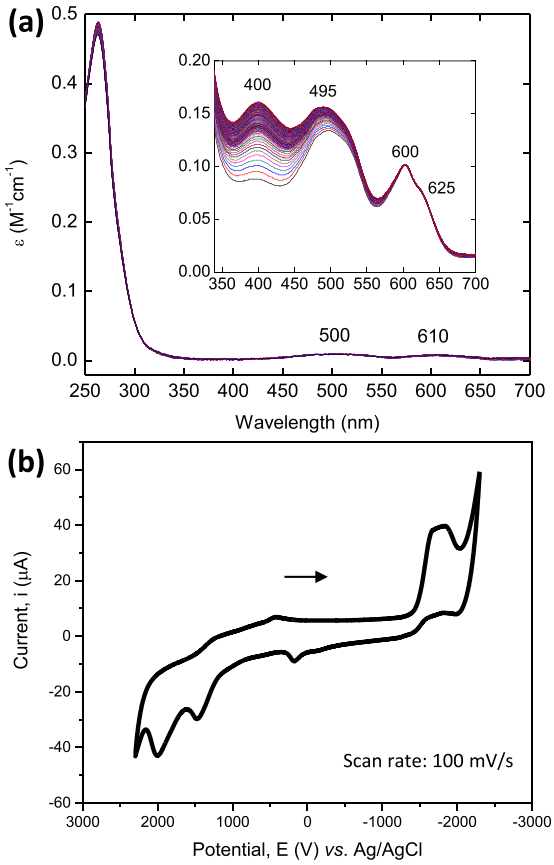

Fig. 1. (a) UV-visible spectra of **1** in 0.1 M aqueous phosphate buffer at pH 11.5. Inset: Stability test over 8h indicating substitution of the apical Cl^- ligand for OH^-. Spectra collected at 300 s intervals; (b) Cyclic voltammogram of **1** recorded in dry acetonitrile at 100 mV/s with 0.1 M $TBAPF_6$ as supporting electrolyte. The solution was purged with inert gas saturated with MeCN vapors for 20 minutes prior to data collection. Experiments utilized a 3-electrode configuration: Hg-pool working electrode; Ag/AgCl (sat'd KCl) reference electrode; Pt wire auxiliary electrode; ferrocene/ferrocenium was used as internal standard and potentials are available in the SI.

An X-band EPR spectrum of **1** in 3:1 DCM:MeCN was taken at 80 K, resulting in a broad signal associated with S = 3/2 attributed to a high spin $3d^7$ configuration (**Fig. S2**). The assignment is straightforward because $3d^6$ $^{LS}Co^{III}$ species with S = 0 are EPR silent, whereas S = ½ $^{LS}Co^{II}$ species with a $3d^7$ configuration tend to be silent at temperatures above 77 K [43]. A DFT comparison of high and low spin configurations for **1** in implicit water showed excellent agreement, and the $3d^7$ $^{HS}Co^{II}$ species was favored by 14 kcal/mol.

The redox behavior of **1** was probed by cyclic voltammetry in MeCN (Figs. 1b**, S3**). A process observed at −1.79 V *vs.* Ag/AgCl is associated with the Co^{II}/Co^{I} couple. This process seems to overlap with a ligand-based $L/L^{\bullet-}$ process at −1.82 V *vs.* Ag/AgCl. Oxidatively, an irreversible Co^{II}/Co^{III} process ($3d^7$ to $3d^6$) occurs at +1.47 V *vs.* Ag/AgCl, and a more positive process at +2.00 V *vs.* Ag/AgCl can be attributed to $L/L^{\bullet+}$.

Electrocatalytic proton reduction. The ability of $[Co^{II}(L^1)Cl]PF_6$ **(1)** to promote proton reduction towards H_2 generation was assessed in MeCN using 0 to 50 equivalents of acetic acid as the proton source (**Fig. S4**). The amplitude of the Co^{II}/Co^{I} process increased upon addition of acid in the first six equivalents. Additional equivalents of acid displaced the wave towards the ligand-based reduction process. This behavior is suggestive of concentration-dependent proton reduction mechanisms, as observed for cobalt oxime catalysts [45]. Bulk electrolysis was performed at an applied potential of −1.70 V *vs.* Ag/AgCl for 3 h in presence of 100 equiv. of acetic acid, to yield a turnover number, TON_{3h}, of 22. This is 45% of the maximum hypothetical TON of 50 expected for this acid load. The charge consumption rate remained high for the first 35 min (*ca.* 2100 s), decreasing sharply afterwards (**Fig. S5**). The rate decrease differs from more gradual processes observed in proton reduction by the Verani Group [44,45] and coincided with a color change from purple to brownish orange. The Faradaic efficiency (%FE) reached up to 79%. These values are within the range we reported previously for other proton reduction catalysts based on oxime and pyridine frameworks. For example, the catalyst $[Co^{III}(prdioxH)(^{4tBu}py)(Cl)]PF_6$, with an N_4 oxime ligand, displayed a comparable TON_{3h} = 19 in presence of trifuoroacetic acid in CH_3CN, with %FE = 80% [46], while the pentadentate N_5 oxime $[Co^{III}(HL)Cl]PF_6$ showed TON_{3h} ~ 15 with %FE of 75% [44]. The structurally closer methylaminopyridine-based catalyst $[Co^{II}(L^2)Cl]ClO_4$ displayed TON_{3h} of 16 in presence of 100 equivalents of acetic acid, and %FE of approximately 90% [45]. The catalyst $[Co^{II}_2(L)(bpy)_2]ClO_4$ with a binucleating amido-based ligand and bipyridines showed a TON_{3h} of 18 with %FE of 94% under similar conditions [47].

Electrocatalytic water reduction. The ability of $[Co^{II}(L^1)Cl]PF_6$ **(1)** to reduce water into H_2 under neutral pH was probed using an H-type cell equipped with Hg-pool, saturated Ag/AgCl and coiled platinum wire as working, reference, and auxiliary electrodes at pH 7. In presence of **1**, considerable current enhancement was observed, as shown in Fig. 2a with a catalytic onset potential −1.59 V *vs.* Ag/AgCl. Taking into account electrolyte pH, the overpotential for H_2 production was calculated it at −0.53 V *vs.* RHE. Controlled potential electrolysis was used to assess quantitatively the catalytic activity of $[Co^{II}(L^1)Cl]PF_6$ **(1).** A potential of −1.70 V *vs.* Ag/AgCl was applied for 3 h, and charge consumption was measured against time. The resulting plot shows a linear increase in charge consumption over the course of the experiment (Fig. 2b).

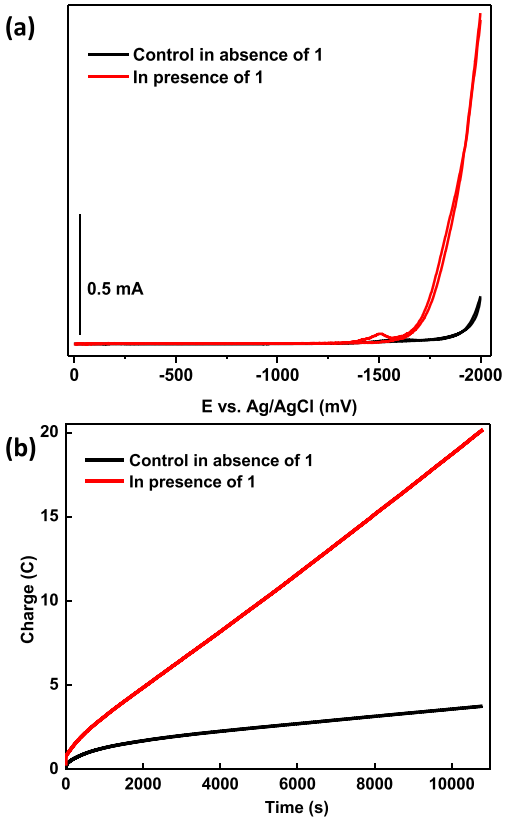

Fig. 2. (a) Electrocatalytic water reduction with $[Co^{II}(L^1)Cl]PF_6$ **(1)** at 100 mV/s scan rate; (b) Charge *vs.* time plot at an applied potential of −1.70 V *vs.* Ag/AgCl at pH 7 (−1.06 V *vs.* RHE). Hg-pool; Ag/AgCl; Pt wire; 1 M phosphate buffer.

Samples of the headspace gas were analyzed as being H_2 by gas chromatography, yielding a TON_{3h} of 390, with associated turnover frequency (TOF) of 130 turnovers per hour. The Faradaic efficiency (%F) reached 80%. Catalyst **1** showed moderate activity when compared to other water-reducing species based on pyridine frameworks [43]. Comparative 12 h bulk electrolysis did not show an increase in charge consumption or in turnover numbers. (**Fig. S6**). The resulting TON_{12h} of 760 reflected a lower TOF of 63 turnovers per hour and Faradaic efficiency of 65%. This behavior indicates catalyst deactivation with likely formation of nanoparticles, which are adsorbed by the Hg pool electrode, and reinforce the notion that the catalyst is molecular. Based on these results, it is possible to speculate that effective water reduction involves the Co^{II}/Co^{I} couple, and that ligand involvement leads to catalyst deactivation over time [24]. This is in good agreement with the expected one-electron reduction of $[Co^{II}(L^1)Cl]^+$ **(1^+)** to form the catalytically active monovalent species $[Co^{I}(L^1)Cl]^o$ or $[Co^{I}(L^1)]^+$ that was sufficiently nucleophilic to react with a proton and form the reactive hydride $[H\text{-}Co^{III}(L^1)]^{2+}$ required for H_2 evolution [48]. Control experiments in absence of the catalyst yielded minimal current enhancement.

Electrocatalytic water oxidation. We assessed water oxidation in aqueous phosphate buffers at pHs 7 and 11.5. Understanding that $[Co^{II}(L^1)Cl]PF_6$ (**1**) features methylene groups prone to oxidation [30,31], we are interested in assessing whether the use of imidazoles as chelators will lead to molecular processes in the first few hours of water oxidation. Enhancement of current associated with catalysis was observed upon anodic scan in both pH ranges in presence of **1**, while control experiments in absence of the catalyst led to only minor current changes in extremely positive potentials. Fig. 3a displays the electrocatalytic water oxidation in presence of 0.18 μmol of **1** at an applied potential of +1.55 V *vs.* Ag/AgCl at pH 7 (+2.19 V *vs.* RHE) while Fig. 3b shows the charge consumption over time. On average, 1.5 e^- are passed per cobalt center to generate the active catalyst. These results reflected the optimization of applied potential and catalyst load described in **Fig. S7**, and led to an average $TON_{3h} = 71$ (TOF 24 h^{-1}) associated with a Faradaic efficiency of *ca.* 65%. At pH 11.5, enhanced activity was observed, in presence of 0.18 μmol of catalyst at an applied potential of +1.20 V *vs.* Ag/AgCl (+2.11 V *vs.* RHE). The applied potential was kept at a moderate value to minimize catalyst decay, and the overpotential is estimated at 0.60 V *vs.* RHE. A TON_{3h} of 103 (TOF 34 h^{-1}) was associated with Faradaic efficiency ≥80% (**Fig. S8**). Comparatively, the reported activities of Co porphyrins [32] have achieved TONs of 90–120, while a dinuclear tmpa-based Co_2 species [40] reached a TON 58. Other catalysts based on Mn ions vary from low activity [49] to TONs between 16 and 25 [50]. A recent article for chlorinated porphyrins reports a TON of 836 [51]. Therefore, the activity of **1** towards water oxidation compares well with other reported catalysts. It is important to note that many of these species had their yields improved by, or were completely dependent on the formation of Co oxide nanoparticles [52,53,54]. Although methylene oxidation, *e.g.* -N–CH_2–Py ➔ -N–C(=O)–Py, is expected to take place over time, these results point to the use of strongly bound imidazoles to enable molecular catalysis in the initial phases of the process.

Resilience of the catalyst. Understanding the usual issues with catalyst degradation over the course of water oxidation, we evaluated the resilience of $[Co^{II}(L^1)Cl]PF_6$ **(1)** to ascertain the nature of the catalyst in the early stages of bulk electrolysis. The pre- and post-catalytic systems were analyzed to probe the molecular stability of the catalyst by means of UV–visible spectroscopy, scanning electron microscopy (SEM), energy dispersive X-ray (EDX), and X-ray photoelectron spectroscopy (XPS) analyses of the FTO working electrodes. At the core of this quest is the determination of whether the catalyst is the molecular species $[Co^{II}(L^1)Cl]PF_6$ **(1)**, or if this species decomposes into nanoparticles that then become catalytic [1,31,32,44]. UV–visible analysis of solutions before and after 3 h bulk electrolysis gave insight to the stability of the molecular species and dynamic light scattering (DLS) was used to detect any water-soluble or delaminated nanoparticles originating from catalyst decomposition. As observed from Fig. 4, excellent agreement between initial and final spectra strongly suggests that **1** remains mostly unaltered during water oxidation at both pHs 7 and 11.5. The ligand-based bands, as well as the metal-based bands, observable at a higher concentration of 5×10^{-4} M, remained intact. Furthermore, the absence of bands at 422 nm and 708 nm associated with the formation of cobalt oxide nanoparticles corroborates the

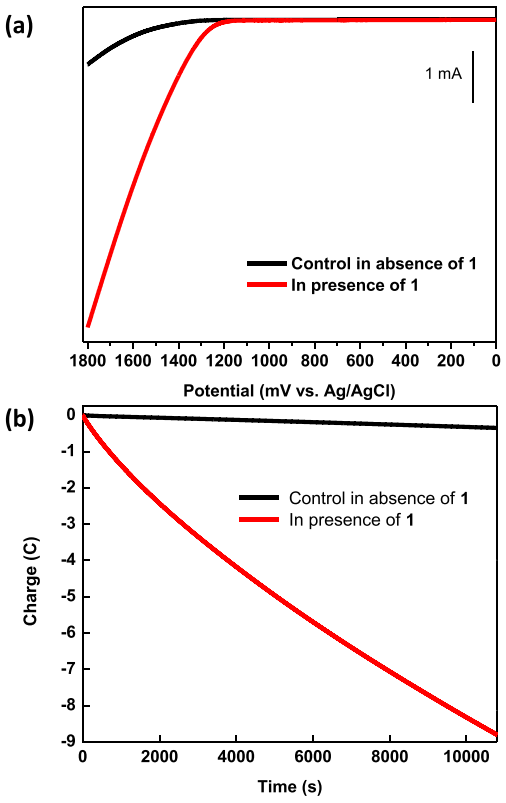

Fig. 3. (a) Electrocatalytic water oxidation with $[Co^{II}(L^1)Cl]PF_6$ **(1)** at 100 mV/s scan rate; (b) Charge *vs.* time plot at an applied potential of +1.55 V *vs.* Ag/AgCl at pH 7 (+2.19 V *vs.* RHE). FTO plate; Ag/AgCl; Pt wire; 1 M phosphate buffer.

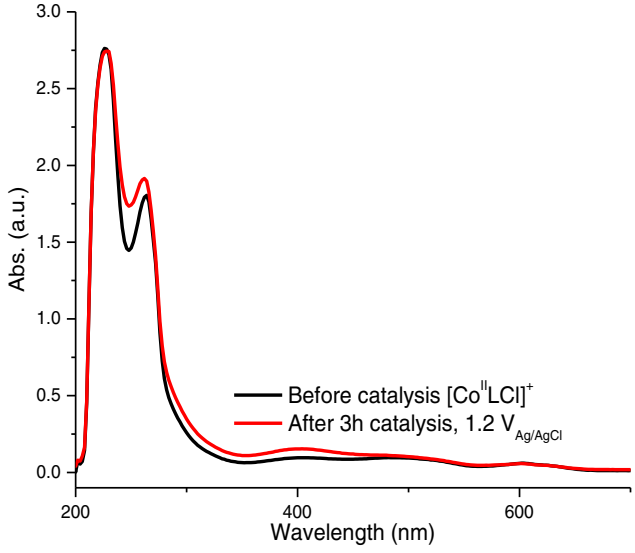

Fig. 4. UV–visible spectrum in 0.1 M phosphate buffer of **1** before catalysis at pH 11.5 (black trace) and after 3 h catalysis (red trace).

molecular nature of the catalyst within that timeframe [55].

This initial molecular stability was further confirmed by SEM analysis of the rinsed FTO working electrode, accompanied by EDX spectroscopy (Fig. 5). In the event of significant catalyst decomposition, the insoluble nanoparticle species would adsorb onto the surface of the electrode and become detectable *via* SEM imaging. However, compared with a control experiment, no distinguishable features were observed. Similarly, the EDX analysis did not support the presence of cobalt within the detection limits of the experiment. DLS experiments were performed after 3 h of controlled potential electrolysis in pH 11.5 at +1.20 V *vs.* Ag/AgCl (+2.11 V *vs.* RHE), using 0.1 M phosphate buffer, and are sensitive to highly scattering structures ranging from sub-nanometer to micron scale. Catalyst-free and catalyst-containing electrolytes have comparable size distributions and low scattering intensities (**Fig. S9**).

Additionally, XPS of the working electrode surface was performed after 3 h of controlled potential electrolysis in pH 11.5 at +1.20 V *vs.* Ag/AgCl (+2.11 V *vs.* RHE), 0.1 M phosphate buffer. High-resolution (HR) spectroscopy targeted cobalt, phosphorus, and tin (Fig. 6). Photoemission lines for Co (2p and 3p) suggest a small amount of Co enrichment under these electrolysis conditions. The binding energies of Co2p bands indicate a 2+ oxidation state. Shake-up satellites characteristic of Co^{2+} are also observed. The spin-orbit split value, *i.e.* the difference between the $Co2p_{3/2}$ and $Co2p_{1/2}$ emission lines, indicates a high spin Co^{2+} species, in good agreement with EPR of the complex. HR-P2p analysis reveals that most surface-confined P exists as P^{5+}, with a binding energy similar to inorganic phosphate. A hypothesized P^{3+} species can be deconvoluted as a minor satellite to the P^{5+} photoemission band. This is attributed to a metal-phosphide decomposition reaction, with a Co:P ratio consistent with cobalt(II) phosphides.

The formation of minuscule nanoparticles in the range 0.5–2 nm has been reported by Fujita et al. [56] and Harriman et al. [57] and cannot be ruled out completely. However, the excellent agreement between UV–visible, SEM, EDX, DLS, and XPS, coupled with considerable water

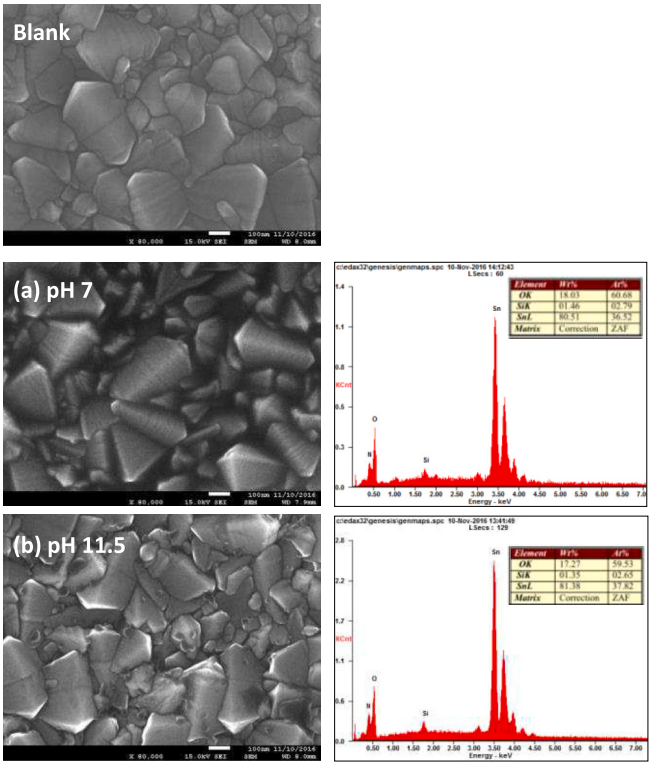

Fig. 5. SEM (80,000× magnified) of used FTO working electrodes (a) at pH 7 and (b) at pH 11.5 after 3 h catalytic oxidation, compared to a used electrode in the absence of **1** (Blank). The EDX distribution on the right indicates absence of cobalt nanoparticles.

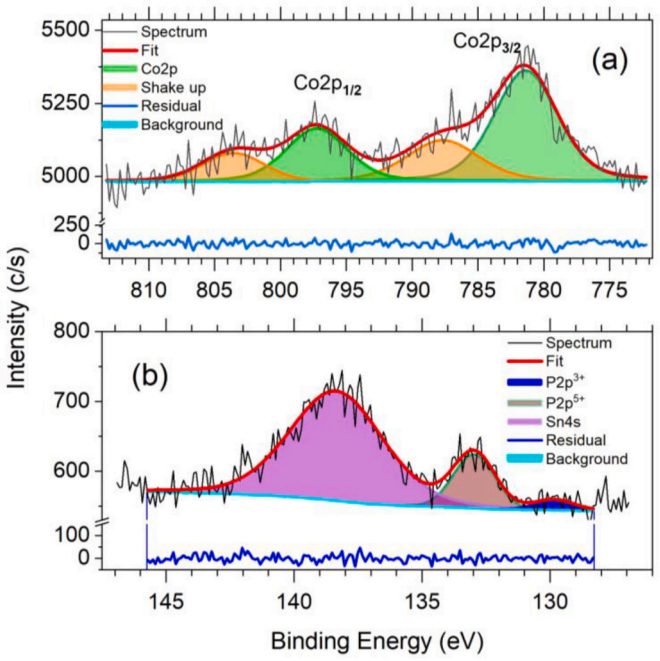

Fig. 6. High-resolution XPS spectra of used FTO working electrodes after 3 h of electrolysis in pH 11.5 buffer: (a) Cobalt 2p, with shake-up satellites characteristic of Co^{2+} (b) Phosphorus 2p, with Tin 4 s deconvoluted at higher binding energy. The majority of phosphorus exists in a + 5 oxidation state, with a binding energy typical of phosphate salts.

oxidation turnovers, surface- and solution-based analyses support the activity of $[Co^{II}(L^1)Cl]PF_6$ (**1**) as molecular during the critical steps of the oxygen-evolving mechanism.

Plausible molecular mechanisms. Viable mechanisms for water oxidation with $[Co^{II}(L^1)Cl]PF_6$ **(1)** were evaluated by density functional theory (DFT) aiming to understand the nature and electronic structure of likely intermediates, and to evaluate the participation of ligand-based and pH-dependent steps at pH 11.5. The results are shown in Fig. 7 with details available in **Figs. S10–12** and **Tables T2-T3**. DFT calculations were based on the published crystal structure [28] and within the constraints of available experimental data. For mechanistic purposes, species **1** is better written in this section as $[(L^1)Co^{II}–Cl]^+$. Replacement of the axial chlorido ligand by an adventitious hydroxide is energetically favored by 13.4 kcal/mol in aqueous media under basic conditions. This replacement leads to the formation of a species described as $[(L^1)Co^{II}–OH]^+$ **(1a)**. This solvated species undergoes a one-electron oxidation (E^o = +0.88 V *vs.* Ag/AgCl) to generate the pro-catalyst $[(L^1)Co^{III}–OH]^{2+}$ **(1b)**. After the formation of this species, a proton-coupled electron transfer (PCET) is proposed to occur, resulting in the oxyl-containing species $[(L^1)Co^{III}–O^{\bullet}]^{2+}$ **(1c)** with an S = 1/2 ground state (E = +0.98 V *vs.* Ag/AgCl) [58]. The low spin state (S = 1/2) is lower in energy than the high spin state (S = 5/2) by about 9 kcal/mol. However, there is an intermediate spin state (S = 3/2) which is slightly more stable than the low spin state by 4.35 kcal/mol. However, this intermediate spin state requires two unpaired electrons on a Co^{III} and an oxyl radical. This configuration is unlikely for a $3d^6$ species, and we have favored the low-spin state Co^{III} species shown in Fig. 7 as the most chemically meaningful. Reaction with a second adventitious OH^- yields a hydroperoxo intermediate described as $[(L^1)Co^{II}–OOH]^+$ **(1d)**, which undergoes another PCET step in order to generate a superoxyl radical intermediate [59] described as $[(L^1)Co^{II}–OO^{\bullet}]^+$ **(1e)**. This intermediate serves as a one-electron source of an energetic diradical species described as $[(L^1)^{HS}Co^{II}–OO^{\bullet\bullet}]^{+2}$ **(1f)**. Dioxygen generation by this $^{HS}Co^{II}$-superoxyl diradical **1f** is favored by about 20 kcal/mol, and makes this step the most exothermic in the overall catalytic pathway.

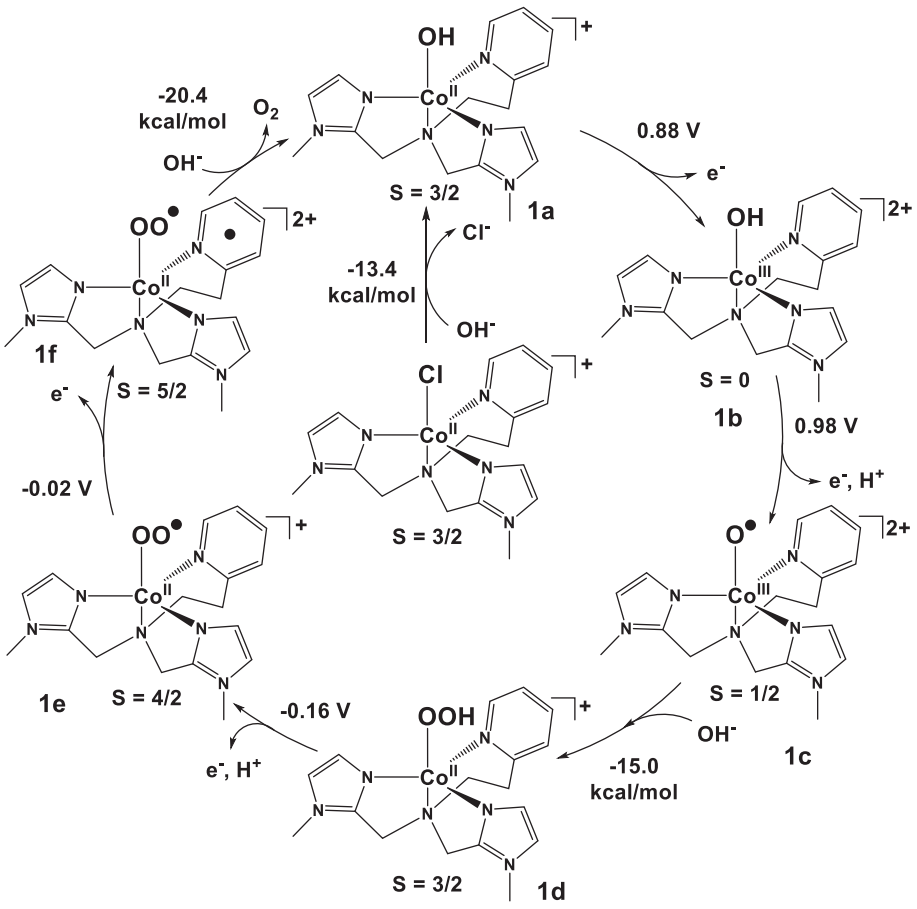

Fig. 7. Plausible initial molecular cycle for O_2 generation by $[Co^{II}(L^1)Cl]PF_6$ **(1)** in water. Optimization with B3LYP* density functional using SDD and 6–31 + G(d,p) basis sets, and SMD-SCRF implicit solvation. Redox potentials for PCET have been calculated at pH = 11.5. Values of potential *vs.* Ag/AgCl.

The metal center does not seem to reach high oxidation states expected for water oxidation, but rather relies on oxygen-centered processes, likely favoring a molecular mechanism. Immediately after O_2 release, the $[(L^1)Co^{II}–OH]^+$ species **1a** is reformed and enables a new catalytic cycle. These calculations do not take into account the aforementioned methylene oxidation, expected to take place in longer catalytic runs.

3. Conclusions

In this paper we investigated the ability of the prototypical redox-activated drug carrier $[Co^{II}(L^1)Cl]PF_6$ **(1)** as a catalyst for water splitting. This imidazole-rich species is structurally comparable to tmpa-based catalysts that decompose during the catalytic cycle. We proposed that the presence of imidazoles would favor low-valent cobalt and preclude dissociation during water reduction, while strong chelation would slow-down ligand degradation during water oxidation. Indeed, this species is capable of water reduction at pH 7 with TON_{3h} 390, and water oxidation at pHs 7 and 11.5 with TON_{3h} of 71 and 103, respectively. The analysis of pre- and post-catalytic solutions confirms that these transformations rely on molecular mechanisms for the initial steps of water oxidation, which proceed *via* a radical-containing superoxyl radical intermediate $[Co^{II}\text{-}OO^{\bullet}]^+$, followed by a diradical species $[Co^{II}\text{-}OO^{\bullet\bullet}]^+$, rather than by the generation of metal-centered high-valent states. This pathway avoids extreme oxidation states that are associated with fast deactivation and demetallation. In conclusion, the use of bio-inspired imidazole-rich environments shows potential for water splitting catalysts.

4. Experimental section

General. Reagents and solvents were used as received from commercial sources. Buffer solutions were prepared on site using ultrapure water (Barnstead NANO pure) with resistivity of 18.2 MΩcm. Infrared spectra were recorded using KBr pellets on a Bruker Tensor 27 FTIR spectrophotometer operating in the range of 4000–450 cm^{-1}. UV–visible spectra were recorded using quartz cells with 1 cm optical pathway at room temperature on a UV3600 Shimadzu UV–Visible-NIR spectrophotometer. Spectra were collected in the range of 190 to 1100 nm, with ε values given in M^{-1} cm^{-1}. ESI-MS in the positive mode was conducted in a Micromass QuattroLC triple quadrupole mass spectrometer with electrospray/APCI source. The continuous wave X-band EPR spectrum of **1** (10^{-3} M) in MeCN was taken at 80 K on a Bruker ELEXSYS E580 EPR spectrometer equipped with an ER 4102ST resonator. Temperature was controlled using a helium gas-flow ICE Oxford cryostat. Elemental analysis (C, H, and N) was performed in a Thermo Scientific FlashEA®1112 Series CHNS/O Elemental Analyzer at the Chemistry Department, Pontifícia Universidade Católica in Rio de Janeiro, Brazil. Aqueous DLS and non-invasive backscattering experiments were performed on a Nano-ZS Zetasizer using disposable zeta potential cells, at the Nanoscale Characterization Facility at Indiana University, Bloomington, US.

Synthesis of $[Co^{II}(L^1)Cl]PF_6$(1). The compound was synthesized as reported [41] by adding a MeOH solution of $CoCl_2{\cdot}6H_2O$ (1 mmol in 15 mL) to a solution of L^1 (1 mmol in 15 mL MeOH) under stirring in a warm water bath. $TBAPF_6$ (2 mmol) was added as a source of counterions after 30 min of reaction, when a purple microcrystalline precipitate started forming. This solid was filtered off, washed with cold MeOH and

diethyl ether and dried under vacuum. Yield: 73%. Anal. Calc. for $C_{17}H_{22}ClCoF_6N_6P$: Calc. C 37.14; H 4.03; N 15.29%. Found: C 37.82; H 3.95; N 15.60%. FTIR in KBr: 3151, 3036, 2957, 1609, 1510, 1463, 1368, 1321, 1165, 1088, 987, 840, 783, 759, 751, 681, 672, 659, 558, 524, 483, 450, 421, 403, 377, 317, 292, 269, 221 cm^{-1}.

Electrochemistry. The electrochemical behavior of complex **1** was studied in a CHI 600 potentiostat/galvanostat. Cyclic voltammograms were obtained at room temperature in MeCN (DriSolv® by MilliporeSigma, > 99.8% anhydrous) solutions containing 0.1 M of tetrabutylammonium hexafluorophosphate ($TBAPF_6$) as the supporting electrolyte under an inert atmosphere. The electrochemical cell was comprised of three electrodes: Glassy carbon or Hg-pool as working electrode (3 mm diameter; 0.071 cm^2), Ag/AgCl as reference electrode, and Pt wire (0.99 mm diameter) as auxiliary electrode. The ferrocenium/ferrocene redox couple (Fc^+/Fc, $E^\circ = 0.40$ V *vs.* NHE) was used as an internal standard [60].

Catalytic studies. Controlled potential electrolysis experiments for complex **1** were performed in a custom-made cell with two compartments of different volume, separated by a frit. The working and reference electrodes were placed in the larger working compartment, while the auxiliary electrode was placed in the adjacent counter compartment. A three-electrode configuration included an Hg-pool or FTO plate working electrode, Ag/AgCl (saturated KCl reference electrode, and a 30 cm long coiled Pt wire auxiliary electrode. Hg-pool working electrodes consisted of an insulated 0.5 mm diameter Pt wire, with an exposed length immersed in a pool of Hg. FTO working electrodes were cut into 2.5 cm^2 plates. *Proton reduction experiments* were performed at room temperature under inert conditions in dry MeCN with $TBAPF_6$ as a supporting electrolyte, using 0 to 50 equivalents of acetic acid (0.1 M in MeCN/$TBAPF_6$) as a proton source. The overpotential was calculated from observed changes in the cyclic voltammogram followed by subtracting the thermodynamic standard potential for H^+/H_2 in MeCN in the presence of HOAc, after considering the homoconjugation effect [61]. *Water reduction experiments* were performed at room temperature and pH 7 under inert conditions using a 1.0 M sodium phosphate buffer. Both chambers were filled with pH 7, 1.0 M phosphate buffer. The major chamber contained 0.18 μmol of **1**. In a typical experiment, the cell was purged with N_2 gas for 20–30 min, followed by gas sampling from the cell headspace (100 μL) to ensure an O_2 free environment by gas chromatography. Then a control solution without catalyst was electrolyzed for 3 h at–1.70 V *vs.* Ag/AgCl. The headspace gas was again injected to the GC to record the amount of adventitious H_2. Then the cell was purged with N_2 gas for another 20 min followed by injection of 0.18 mmol of **1**. The catalyst-containing solution was bulk electrolyzed for another 3 h, and 100 μL headspace gas was injected to the gas chromatograph to record the amount of H_2 produced. The turnover number was calculated after background subtraction as the ratio between moles of H_2 produced over moles of catalyst used. Faradaic efficiency was calculated from gas chromatographic measurements. *Water oxidation experiments* were performed in aqueous phosphate buffer solutions at pHs 7 (1.0 M) and 11.5 (0.1 M). These aqueous buffers use atmospheric O_2/N_2 as the internal standard. Experiments were optimized for catalyst load at 0.09 and 0.18 μmol of **1**. Reported results in this paper use the higher catalyst load. For catalytic studies, 100 μL of the headspace in the electrochemical cell were sampled by gas chromatography from a blank solution of 35 mL pH 7 and 11.5 phosphate buffer and compared with 100 μL of atmospheric O_2 and N_2. In the absence of the catalyst, O_2 levels are comparable to atmospheric measurements. However, in the presence of **1**, O_2 levels considerably increased compared to the control. The amount of gas produced in all experiments was determined with a Gow-Mac 400 gas chromatograph equipped with a thermal conductivity detector, and a 8 ft. x 1/8 in, 5 Å molecular sieve column operating at a temperature of 60° C. Nitrogen was used as carrier gas for H_2 detection at a flow rate of 30 mL min^{-1} using a calibration curve. Helium was used as carrier gas for O_2 detection.

X-ray Photoelectron Spectroscopy (XPS). XPS experiments were conducted by a PHI VersaProbe II instrument equipped with a focused monochromatic Al Kα source. XPS spectra were acquired under ultra-high vacuum (*ca.* 8×10^{-10} Torr), with an X-ray power of 25 W at 15 kV, and a 100 μm beam size at the take-off angles of 45° and normal X-ray incidence. The instrument work function was calibrated to give a binding energy of 84.0 eV for the Au $4f_{7/2}$ photoemission line in metallic gold. The spectrometer dispersion was adjusted to give respective binding energies of 284.8 eV for the C 1 s photoemission line of adventitious (aliphatic) carbon on non-sputtered samples; 932.7 eV for the Cu $2p_{3/2}$ line; and 368.3 eV for the Ag $3d_{5/2}$ line. The PHI dual-charge neutralization system was used on all samples. High resolution Co2p, Co3p, P2p and C1s spectra were taken with a minimum of 25–60 scans using 0.1 eV steps and 93.9, 46.9, 23.5 eV pass energy for Co, P and C, correspondingly. All XPS spectra were recorded using PHI software SmartSoft–XPS v2.6.3.4, and processed using PHI MultiPack v9.3.0.3 and/or CasaXPS v.2.3.14 using Shirley background. Atomic percentages were determined using relative sensitivity factors from the MultiPack library. Peaks were fitted using GL line shapes, *i.e.* a combination of Gaussians and Lorentzians. Each sample was examined at 5–6 different areas on the mounted specimen to ensure consistent, reproducible spectra. All high-resolution spectra were calibrated in respect to the C1s photoemission line of adventitious (aliphatic) carbon.

Computational Methods. Electronic structure calculations for complex **1** and its associated species were performed using the Gaussian (G09) package [62]. The geometries were optimized starting from an existing X-ray structure using B3LYP* density functional [63,64,65] with SDD basis set and effective core potential (ECP) [66,67] for the cobalt atom and 6–31 + G(d,p) [68,69,70] basis set for all the other atoms. The aqueous solvent environment was modelled with SMD-SCRF [71] implicit solvation, included in all geometry optimizations. Optimized geometries were confirmed as minima on the potential energy by vibrational frequency calculations and had no imaginary frequencies. The converged wavefunctions were tested and confirmed to be stable. Thermal and entropy contributions to the free energy were calculated by using unscaled B3LYP* frequencies and rigid rotor/harmonic oscillator approximations at 298.15 K. For a redox reaction, $\mathbf{X_{(aq)} \rightarrow X^{n+}_{(aq)} + ne^-_{(aq)}}$, the standard redox potential is given by:

$$E^o_{(aq)} = \frac{-\Delta G^*_{(aq)}}{nF} - SHE$$

where $\Delta G_{(aq)}^* = G_{X,\,(aq)}^* - G_{X^{n+},\,(aq)}^* - G_{e,\,(g)}^*$ is the standard free energy change for a redox reaction in aqueous solution. $G_{e(g)}^* = 0.867$ kcal/mol is the free energy of electron at 298.15 K, obtained from literature [72]. The Faraday constant F is 23.06 kcal/(mol V), and n is the number of electrons, with SHE being the absolute potential of standard hydrogen electrode (4.281 V) [73].

For the reactions involving proton-coupled electron transfer (PCET), the aqueous phase free energy of proton was calculated by using:

$$G^*_{H^+,(aq)} = G^o_{H^+,(g)} + \Delta G^*_{solv,(aq)} + \Delta G^{1atm\rightarrow 1M}$$

where $G_{H^+,\,(g)}^o = -6.29$ kcal/mol at 298.15 K is derived from $G_{H^+,\,(g)}^o = H^o_{(g)} - TS^o_{(g)}$, with $H^o_{(g)} = 1.48$ kcal/mol and $S^o_{(g)} = 26.05$ cal/(mol K), $\Delta G_{solv,\,(aq)}^* = -265.9$ kcal/mol is the solvation energy of the proton, as taken from the literature [74,75] and $\Delta G^{1atm\rightarrow 1M} = 1.89$ kcal/mol is the correction to the free energy for changing from the standard state of 1 atm to 1 M [76]. Since the experiments are performed at pH 11.5, the computed standard redox potentials are adjusted to the experimental pH conditions using the Nernst equation:

$$E^{pH}_{(aq)} = E^o_{(aq)} - \frac{RT\ ln(10)}{n_{e^-}} \times n_{H^+} \times pH$$

where, n_{e^-} and n_{eH^+} are the number of electrons and protons, respectively. The gas constant is $R = 1.987$ cal/mol K and T is the temperature ($T = 298.15$ K).

CRediT authorship contribution statement

Krista M. Kulesa: Formal analysis, Investigation, Writing – original draft. **Diego S. Padilha:** Formal analysis, Investigation, Writing – original draft. **Bishnu Thapa:** Formal analysis, Investigation, Writing – original draft. **Shivnath Mazumder:** Formal analysis, Validation, Writing - original draft. **H. Bernhard Schlegel:** Data curation, Funding acquisition, Methodology, Resources, Supervision, Writing – review & editing. **Marciela Scarpellini:** Data curation, Funding acquisition, Methodology, Resources, Supervision, Writing – review & editing. **Cláudio N. Verani:** Conceptualization, Data curation, Funding acquisition, Methodology, Project administration, Resources, Supervision, Validation, Writing - original draft, Writing - review & editing.

Declaration of Competing Interest

The authors declare that they have no known competing financial interests or personal relationships that could have appeared to influence the work reported in this paper.

Data availability

Data will be made available on request.

Acknowledgements

Prof. Ademir Neves (1951-2022) was the advisor of Marciela Scarpellini (Ph.D.2001) and Cláudio N. Verani (M.Sc.1996). With this joint effort the authors express their appreciation towards his mentorship and scientific legacy. This research was sponsored by the Division of Chemical Sciences, Geosciences, and Biosciences, Office of Basic Energy Sciences of the U.S. Department of Energy through the Solar Energy program under grants DE-SC-00022114 to CNV and DE-SC0001907 to CNV and HBS, as well as the National Science Foundation grant CHE-1464450 to HBS. MS acknowledges the Coordenação de Aperfeiçoamento de Pessoal de Nível Superior – CAPES (Brazil) under grant 3100.101.7006-P6 and a PhD stipend to DSP from the Conselho Nacional de Pesquisa - CNPq (Brazil) managed by the UFRJ. SM acknowledges the start-up provided by IIT Jammu and a grant from the Council of Scientific and Industrial Research - CSIR (India) 01(3047)/21/EMR-II for support. Technical assistance is acknowledged to Prof. Ricardo Aucélio at the Pontifícia Universidade Católica – Rio de Janeiro on elemental analyses, to Dr. Oleg Poluektov and Dr. Jens Niklas at the Argonne National Laboratories on the EPR data, and to Mr. Mackenzie Fahey at Indiana University on DLS measurements. Prof. Long Luo at WSU is acknowledged for discussions pertaining the electrochemistry of these species.

Appendix A. Supplementary data

Supplementary data to this article can be found online at https://doi.org/10.1016/j.jinorgbio.2023.112162.

References

[1] K.E. Dalle, J. Warnan, J.J. Leung, B. Reuillard, I.S. Karmel, E. Reisner, Chem. Rev. 119 (2019) 2752–2875.
[2] K.J. Young, B.J. Brennan, R. Tagore, G.W. Brudvig, Acc. Chem. Res. 48 (2015) 567–574.
[3] L. Duan, L. Wang, F. Li, F. Li, L. Sun, Acc. Chem. Res. 48 (7) (2015) 2084.
[4] J.J. Concepcion, J.W. Jurss, M.K. Brennaman, P.G. Hoertz, A.O.T. Patrocinio, N.Y. M. Iha, J.L. Templeton, T.J. Meyer, Acc. Chem. Res. 42 (2009) 1954.
[5] C.W. Cady, R.H. Crabtree, G.W. Brudvig, Coord. Chem. Rev. 252 (2008) 444–455.
[6] M. del Barrio, M. Sensi, C. Orain, C. Baffert, S. Dementin, V. Fourmond, C. Léger, Acc. Chem. Res. 51 (2018) 769–777.
[7] W.T. Eckenhoff, Coord. Chem. Rev. 373 (2018) 295–316.
[8] (a) Z. Han, R. Eisenberg, Acc. Chem. Res. 47 (2014) 2537–2544; (b) J.R. McKone, S.C. Marinescu, B.S. Brunschwig, J.R. Winkler, H.B. Gray, Chem. Sci. 5 (2014) 865–878.
[9] M. Wang, L. Chen, L. Sun, Energy Environ. Sci. 5 (2012) 6763–6778.
[10] X. Zhao, P. Wang, M. Long, Comm. Inorg. Chem. 37 (2017) 238–270.
[11] V.S. Thoi, Y. Sun, J.R. Long, C.J. Chang, Chem. Soc. Rev. 42 (2013) 2388–2400.
[12] R.M. Bullock, A.M. Appel, M.L. Helm, Chem. Commun. 50 (2014) 3125–3143.
[13] (a) S. Barnett, K. Goldberg, J.A. Mayer, Nat. Chem. 4 (2012) 498–502; (b) D.L. Gerlach, S. Bhagan, A.A. Cruce, D.B. Burks, I. Nieto, H.T. Truong, S. P. Kelley, C.J. Herbst-Gervasoni, K.L. Jernigan, M.K. Bowman, S. Pan, M. Zeller, E. T. Papish, Inorg. Chem. 53 (2014) 12689–12698; (c) T. Zhang, C. Wang, S. Liu, J.-L. Wang, W. Lin, J. Am. Chem. Soc. 136 (1) (2014) 273–281.
[14] S. Mandal, S. Shikano, Y. Yamada, Y.-M. Lee, W. Nam, A. Llobet, S. Fukuzumi, J. Am. Chem. Soc. 135 (2013) 15294–15297.
[15] A.E. King, Y. Surendranath, N.A. Piro, J.P. Bigi, J.R. Long, C.J. Chang, Chem. Sci. 4 (2013) 1578–1587.
[16] P.H.A. Kankanamalage, S. Mazumder, V. Tiwari, K.K. Kpogo, H.B. Schlegel, C. N. Verani, Chem. Commun. 52 (2016) 13357–13360.
[17] D.M. Ekanayake, K.M. Kulesa, J. Singh, K.K. Kpogo, S. Mazumder, H.B. Schlegel, C. N. Verani, Dalton Trans. 46 (2017) 16812–16820.
[18] B.H. Solis, S. Hammes-Schiffer, J. Am. Chem. Soc. 133 (2011) 19036–19039.
[19] S.G. Patra, A. Mizrahi, D. Meyerstein, Acc. Chem. Res. 53 (2020) 2189–2200.
[20] S. Fukuzumi, T. Kojima, Y.-M. Lee, W. Nam, Coord. Chem. Rev. 333 (2017) 44–56.
[21] T.K. Michaelos, D.Y. Shopov, S.B. Sinha, L.S. Sharninghausen, K.J. Fisher, H.M. C. Lant, R.H. Crabtree, G.W. Brudvig, Acc. Chem. Res. 50 (2017) 952–959.
[22] C. Lu, J. Wang, Z. Chen, ChemCatChem 8 (2016) 2165–2170.
[23] L.D. Wickramasinghe, R. Zhou, R. Zong, P. Vo, K.J. Gagnon, R.P. Thummel, J. Am. Chem. Soc. 137 (2015) 3260.
[24] A.R. Parent, K. Sakai, ChemSusChem 7 (2014) 2070–2080.
[25] A. Singh, L. Spiccia, Coord. Chem. Rev. 257 (2013) 2607–2622.
[26] M.-T. Zhang, Z. Chen, P. Kang, T.J. Meyer, J. Am. Chem. Soc. 135 (2013) 2048–2051.
[27] M.D. Kärkäs, B. Åkermark, Dalton Trans. 45 (2016) 14421–14461.
[28] C. Casadevall, V. Martin-Diaconescu, W.R. Browne, S. Fernández, F. Franco, N. Cabello, J. Benet-Buchholz, B. Lassalle-Kaiser, J. Lloret-Fillol, Nat. Chem. 13 (2021) 800–804.
[29] C.J. Ballhausen, Introduction to Ligand Field Theory, 1st edition, McGraw Hill, 1962.
[30] B.N. Figgis, M.A. Hitchman, Ligand Field Theory and Its Applications, 1st edition, Wiley-VCH, 1999.
[31] S. Fukuzumi, Y.-M. Lee, W. Nam, Dalton Trans. 48 (2019) 779–798.
[32] P. Garrido-Barros, C. Gimbert-Suriñach, R. Matheu, X. Sala, A. Llobet, Chem. Soc. Rev. 46 (2017) 6088–6098.
[33] C.-F. Leung, S.-M. Ng, C.-C. Ko, W.-L. Man, J. Wu, L. Chen, T.-C. Lau, Energy Environ. Sci. 5 (2012) 7903–7907.
[34] (a) L.-Z. Fu, L.-L. Zhou, S.-Z. Zhan, RSC Adv. 5 (2015) 42287–42293; (b) L.-Z. Fu, T. Fang, L.-L. Zhou, S.-Z. Zhan, RSC Adv. 4 (2014) 53674–53680.
[35] H. Baydoun, S. Mazumder, H.B. Schlegel, C.N. Verani, Chem. Eur. J. 23 (2017) 9266–9271.
[36] H.-Y. Du, S.-C. Chen, X.-J. Su, L. Jiao, M.-T. Zhang, J. Am. Chem. Soc. 140 (2018) 1557–1565.
[37] H. Baydoun, J. Burdick, B. Thapa, L. Wickramasinghe, D. Li, J. Niklas, O. G. Poluektov, H.B. Schlegel, C.N. Verani, Inorg. Chem. 57 (2018) 9748–9756.
[38] K. Koshiba, K. Yamauchi, K. Sakai, Angew. Chem. Int. Ed. 56 (2017) 4247–4251.
[39] B.M. Pires, L.C. Giacomin, F.A.V. Castro, A.S. Cavalcanti, M.D. Pereira, A. J. Bortoluzzi, R.B. Faria, M. Scarpellini, J. Inorg. Biochem. 157 (2016) 104–113.
[40] (a) G.B. Wijeratne, S. Hematian, M.A. Siegler, K.D. Karlin, J. Am. Chem. Soc. 139 (2017) 13276–13279; a E.E. Chufán, S.C. Puiu, K.D. Karlin, Acc. Chem. Res. 40 (2007) 563–572; b K.D. Karlin, S. Kaderli, A.D. Zuberbühler, Acc. Chem. Res. 30 (1997) 139–147; c R.R. Jacobson, Z. Tyeklar, A. Farooq, K.D. Karlin, S. Liu, J. Zubieta, J. Am. Chem. Soc. 110 (1988) 3690–3692.
[41] H.Y. Wang, E. Mijangos, S. Ott, A. Tapper, Angew. Chem. Int. Ed. 53 (2014) 14499–14502.
[42] M. Scarpellini, J.C. Toledo, A. Neves, J. Ellena, E.E. Castellano, D.W. Franco, Inorg. Chim. Acta 357 (2004) 707–715.
[43] R. Shakya, S.S. Hindo, L. Wu, M.M. Allard, M.J. Heeg, H.P. Hratchian, B. R. McGarvey, S.R.P. da Rocha, C.N. Verani, Inorg. Chem. 46 (2007) 9808–9818.
[44] D. Basu, S. Mazumder, X. Shi, R.J. Staples, H.B. Schlegel, C.N. Verani, Angew. Chem. Int. Ed. 54 (2015) 7139–7143.
[45] D. Basu, S. Mazumder, X. Shi, H. Baydoun, J. Niklas, O. Poluektov, H.B. Schlegel, C. N. Verani, Angew. Chem. Int. Ed. 54 (2015) 2105–2110.
[46] D. Basu, S. Mazumder, J. Niklas, H. Baydoun, D. Wanniarachchi, X. Shi, R. J. Staples, O. Poluektov, H.B. Schlegel, C.N. Verani, Chem. Sci. 7 (2016) 3264–3278.
[47] K.K. Kpogo, S. Mazumder, D. Wang, H.B. Schlegel, A.T. Fiedler, C.N. Verani, Chem. Eur. J. 23 (2017) 9272–9279.
[48] A. Lewandowska-Andralojc, T. Baine, X. Zhao, J.T. Muckerman, E. Fujita, D. E. Polyansky, Inorg. Chem. 54 (2015) 4310–4321.
[49] K.J. Young, M.K. Takase, G.W. Brudvig, Inorg. Chem. 52 (2013) 7615–7622.
[50] W.-T. Lee, S.B. Muñoz, D.A. Dickie, J.M. Smith, Angew. Chem. Int. Ed. 53 (2014) 9856–9859.
[51] T. Nakazono, K. Sakai, Dalton Trans. 45 (2016) 12649–12652.
[52] J.-W. Wang, P. Sahoo, T.-B. Lu, ACS Catal. 6 (2016) 5062.
[53] D. Hong, S. Mandal, Y. Yamada, Y.-M. Lee, W. Nam, A. Llobet, S. Fukuzumi, Inorg. Chem. 52 (2013) 9522.
[54] G. Chen, L. Chen, S.-M. Ng, W.-L. Man, T.-C. Lau, Angew. Chem. Int. Ed. 52 (2013) 1789.

[55] X. He, W. Zhong, S. Yan, C. Liu, H. Shi, C.-T. Au, Y. Du, J. Phys. Chem. C 118 (2014) 13898–13903.
[56] A. Lewandowska-Andralojc, D.E. Polyansky, C.-H. Wang, W.-H. Wang, Y. Himeda, E. Fujita, Phys. Chem. Chem. Phys. 16 (2014) 11976–11987.
[57] G.S. Nahor, P. Hapiot, P. Neta, A. Harriman, J. Phys. Chem. 95 (2) (1991) 616–621.
[58] D.W. Crandell, S. Ghosh, C.P. Berlinguette, M.-H. Baik, ChemSusChem 8 (2015) 844–852.
[59] A. Moysiadou, S. Lee, C.-S. Hsu, H.M. Chen, X. Hu, J. Am. Chem. Soc. 142 (2020) 11901–11914.
[60] R.R. Gagne, C.A. Koval, G.C. Lisensky, Inorg. Chem. 19 (1980) 2854–2855.
[61] V. Fourmond, P.-A. Jacques, M. Fontecave, V. Artero, Inorg. Chem. 49 (2010) 10338–10347.
[62] M.J. Frisch, G.W. Trucks, H.B. Schlegel, G.E. Scuseria, M.A. Robb, J.R. Cheeseman, G. Scalmani, V. Barone, G.A. Petersson, H. Nakatsuji, X. Li, M. Caricato, A. Marenich, J. Bloino, B.G. Janesko, R. Gomperts, B. Mennucci, H.P. Hratchian, J. V. Ortiz, A.F. Izmaylov, J.L. Sonnenberg, D. Williams-Young, F. Ding, F. Lipparini, F. Egidi, J. Goings, B. Peng, A. Petrone, T. Henderson, D. Ranasinghe, V. G. Zakrzewski, J. Gao, N. Rega, G. Zheng, W. Liang, M. Hada, M. Ehara, K. Toyota, R. Fukuda, J. Hasegawa, M. Ishida, T. Nakajima, Y. Honda, O. Kitao, H. Nakai, T. Vreven, K. Throssell, J.A. Montgomery, J.E. Peralta Jr, F. Ogliaro, M. Bearpark, J.J. Heyd, E. Brothers, K.N. Kudin, V.N. Staroverov, T. Keith, R. Kobayashi, J. Normand, K. Raghavachari, A. Rendell, J.C. Burant, S.S. Iyengar, J. Tomasi, M. Cossi, J.M. Millam, M. Klene, C. Adamo, R. Cammi, J.W. Ochterski, R.L. Martin, K. Morokuma, O. Farkas, J.B. Foresman, D.J. Fox, Gaussian Version G09, Revision E01, 2016.
[63] A.D. Becke, Phys. Rev. A 38 (1988) 3098–3100.
[64] C. Lee, W. Yang, R.G. Parr, Phys. Rev. B 37 (1988) 785–789.
[65] A.D. Becke, J. Chem. Phys. 98 (1993) 5648–5652.
[66] T.H. Dunning Jr., P.J. Hay, in: H.F. Schaefer III (Ed.), Modern Theoretical Chemistry, Plenum, New York, 1977, pp. 1–28.
[67] U.D.H. Andrae, M. Dolg, H. Stoll, H. Preuss, Theoret. Chim. Acta 77 (1990) 123–141.
[68] R. Ditchfield, W.J. Hehre, J.A. Pople, J. Chem. Phys. 54 (1971) 724–728.
[69] W.J. Hehre, R. Ditchfield, J.A. Pople, J. Chem. Phys. 56 (1972) 2257–2261.
[70] M.M. Francl, W.J. Pietro, W.J. Hehre, J.S. Binkley, M.S. Gordon, D.J. DeFrees, J. A. Pople, J. Chem. Phys. 77 (1982) 3654–3665.
[71] A.V. Marenich, C.J. Cramer, D.G. Truhlar, J. Phys. Chem. B 113 (2009) 6378–6396.
[72] J.E. Bartmess, J. Phys. Chem. 99 (1995) 6755.
[73] A.A. Isse, A. Gennaro, J. Phys. Chem. B 114 (2010) 7894–7899.
[74] D.M. Camaioni, C.A. Schwerdtfeger, J. Phys. Chem. A 109 (2005) 10795–10797.
[75] C.P. Kelly, C.J. Cramer, D.G. Truhlar, J. Phys. Chem. B 110 (2006) 16066–16081.
[76] A. Ben-Naim, Y. Marcus, J. Chem. Phys. 81 (1984) 2016–2027.